Quantifying delta channel network changes with Landsat time-series data

Chunpeng Chen[a], Bo Tian[a], Christian Schwarz[b], Ce Zhang[c], Leicheng Guo[a], Fan Xu[a], Yunxuan Zhou[a], Qing He[a]

[a]State Key Laboratory of Estuarine and Coastal Research, East China Normal University, Shanghai, 200241, China

[b]School of Marine Science and Policy, University of Delaware, Lewes, 19958, DE, USA

[c]Lancaster Environment Centre, Lancaster University, Lancaster LA1 4YQ, UK

Corresponding author: Bo Tian (btian@sklec.ecnu.edu.cn)

Abstract: Delta channel networks (DCNs) are highly complex and dynamic systems that are governed by natural and anthropogenic perturbations. Challenges remain in quickly quantifying the length, width, migration, and pattern changes of deltaic channels accurately and with a high frequency. Here, we develop a quantitative framework, which introduces a water occurrence algorithm based on Landsat time-series data and spatial morphological delineation methods, in order to measure DCN structures and associated changes. In examining the Pearl River Delta (PRD) and Irrawaddy River Delta (IRD) as case studies, we analyze their conditions and trends between 1986–2018 at ten-year intervals. Both study areas have undergone various human interventions, including dam construction, sand mining, and land use change driven by urbanization. Our results show the following: (1) the use of a 0.5 water occurrence extraction based on Landsat time-series data, morphological delineation, and spatial change analysis methods can quantify the morphodynamics of DCNs effectively with a root-mean-square error of 15.1 m; (2) there was no evident channel migration in either PRD or IRD with average channel widths of 387.6 and 300.9 m, respectively. Most channels in the PRD underwent remarkable shrinkage, with average rates of 0.4–6.4 m/year, while there were only slight changes in the IRD, which is consistent with observed trends in sediment load variation. The results of this research have the potential to contribute to sustainable river management in terms of flood prevention, riparian tideland reclamation, and water and sediment regulation. Moreover, the proposed framework can be used to develop a new global river width dataset and can be generalized to remotely sensed water discharge and river depth estimation.

Keywords: Delta channel network; Landsat time-series; Channel width; Channel migration; Remote sensing

1. Introduction

Delta channel networks (DCNs) are the backbone of river deltas and form essential pathways for water, sediment, organic matter, and nutrient fluxes from continents to oceans. The structure of DCNs and spatial changes in their channel width, depth, length, and sinuosity have a significant impact on hydrodynamics and sediment transport processes (Syvitski et al., 2005). Variations in water and sediment discharge, riparian vegetation, rate of sea-level rise, waves, and tides can all alter both channel locations and widths through lateral migration. They can even initiate new bifurcations and reorganize structural network patterns (Abed-Elmdoust et al., 2016; Gugliotta and Saito, 2019; Syvitski et al., 2009; Willett et al., 2014).

Global-scale accelerations in sea-level rise rates and increased frequencies of extreme events (e.g., storm surges and extreme precipitation) have become a global concern due to heightened coastal flood risk and accompanied damage to coastal infrastructure and populations

(Kulp and Strauss, 2019; Rahmstorf, 2017). To better protect densely populated low-lying coastal areas from flooding, an increasing number of the world's deltaic channels have been fixed by constructing dikes, embankments, and sluice gates. For example, more than 4600 km of levees and floodwalls have been built along the Mississippi River system (Remo et al., 2018). The river channels in the Pearl River Delta (PRD) have been significantly altered by levee construction since the 1980s (Zhang et al., 2009). These forms of hard infrastructure significantly influence both channel morphology and depositional environments, which can result in increased channel incision and deepening especially under conditions of reduced sediment load in the upstream portions of the delta (Lu et al., 2007; Mei et al., 2018). They can also cause increased sediment deposition and riverbed rise near the delta mouth due to the presence of backwater and the top-lifted effect of sea-level rise (Remo et al., 2018; Syvitski et al., 2009; Wang and Xu, 2018). Moreover, due to both increasing human activities (especially upstream dam construction, which can result in a rapid decline of water flow and sediment discharge) and natural factors (e.g., sea-level rise due to global climate change), DCNs are changing more rapidly at the multi-decade timescale within most of the world's deltas (Liu et al., 2019; Syvitski et al., 2009). Therefore, an efficient method to quantitatively measure the conditions and trends of DCNs is crucial in understanding the role of human activity and climate change on DCN adaptations and to assess sustainable delta development.

The effectiveness of inferring channel delineation from digital terrain maps utilizing topographic signatures (e.g., slope) from synthetic aperture radar (SAR) imagery and from multispectral/hyperspectral remotely sensed imagery has been widely demonstrated in previous studies (Klemenjak et al., 2012; Passalacqua et al., 2010). Yamazaki et al. (2014) constructed a global database for the width of large rivers with a 300-m spatial resolution based on the SRTM Water Body Data and the HydroSHEDS flow direction maps. Database quality strongly depends on the availability of global surface water body data and cannot be efficiently applied to the study of channel morphology changes. Obida et al. (2019) utilized multi-temporal Sentinel-1 SAR data for raster- and vector-based river network delineation using unsupervised classification techniques and thinning algorithms. However, this river network delineation approach introduces increased uncertainty in estuarine areas where the SAR backscattering coefficients are generally similar because of the comparable surface roughness of flat banks and adjacent water bodies (Lee et al., 2011).

The spectral characteristics of surface water with a low absorption in the green band and high absorption in the near and shortwave infrared bands are helpful to differentiate water from other land cover classes. Therefore, optical remote sensing images have been widely utilized for river network extraction using automatic (Isikdogan et al., 2017; Monegaglia et al., 2018; Pavelsky and Smith, 2008; Schwenk et al., 2017) or semi-automatic approaches (Chen et al., 2020b; Gong et al., 2020; Rowland et al., 2016). The common strategy behind these optical methods was to first enhance the contrast between the water bodies and other forms of land cover using water indexes, such as the Normalized Difference Water Index (NDWI) (McFeeters, 1996), the Modified Normalized Difference Water Index (MNDWI) (Xu, 2006), and the Automated Water Extraction Index (AWEI) (Feyisa et al., 2014). From there, morphological algorithms (Gong et al., 2020; Isikdogan et al., 2015; Jarriel et al., 2019; Yang et al., 2015) or machine learning classification algorithms (Li et al., 2019; Yang et al., 2014) were used to extract the rivers. The RivaMap software developed by Isikdogan et al. (2017) facilitates the delineation of rivers by applying a singularity index in a fully automated manner; however, this algorithm interrupts the connectivity of river boundaries. A method proposed recently by Chen et al. (2020b) partly addressed this limitation by using a path tracking technique to delineate connected river networks, however, such a method may fail to delineate meandering rivers because the cost of a path through nearby linear rivers is less than that of a path through the meandering river. Several previous studies have specifically addressed the issue of the extraction and analysis of extremely dynamic meandering rivers (Monegaglia et al., 2018; Rowland et al., 2016; Shahrood et al., 2020).

These existing studies mentioned above, however, require adjustments when applied in delineating deltaic channel networks due to the effects of time-varying water discharge and tides, as such, they could not provide a set of consistent criteria for extracting and quantifying DCNs. This has limited their real-world application in the study of deltaic system evolution. To address this gap, this study aims to develop a quantitative methodological framework to delineate and explore the spatial and temporal changes of DCNs from Landsat time-series data. Our methodology is innovative in making use of a specific water occurrence (i.e., 0.5) derived from Landsat time-series images as a measure of deltaic channel dynamics over a given time period. This method was applied to two tropical river deltas: the PRD in China and Irrawaddy River Delta (IRD) in Myanmar; each with different levels of human activity relative to their changing deltaic patterns from 1986 to 2018.

2. Study areas

We selected the PRD (Fig. 1a) in China and the IRD (Fig. 1b) in Myanmar as reference cases because both deltas are densely populated and characterized by intricate channel networks, which experience different anthropogenic stresses throughout their river basins. The Pearl River basin is located in both tropical and sub-tropical climate zones, with annual mean temperatures ranging from 14 °C to 22 °C and an annual average precipitation of 1525.1 mm (Zhang et al., 2012). The PRD has a catchment area of 425,000 km^2 with three major tributaries: the West River, the North River, and the East River. Annually, approximately 88 million tons (Mt) of sediment and 330 km^3 of water are discharged into the South China Sea through eight river outlets. The mean tidal range in the Pearl River estuary is 1.0–1.7 m. In addition, the PRD hosts a population of 24 million and ranks amongst the fastest growing deltas with respect to economic growth and urbanization in the world. More than 14,000 dams and reservoirs have been built on the Pearl River basin since 1980 and fixed levees have been constructed along most of its channels (Wu et al., 2018).

The Irrawaddy River basin has a tropical monsoon climate with an average annual temperature ranging from 19 to 31 °C and a mean annual precipitation of between ∼500 mm and ∼4000 mm (Sirisena et al., 2018). The Irrawaddy River is the most important river for commercial navigation in Myanmar and it enters into the Andaman Sea through twelve river outlets, forming one of the largest deltaic systems in Southeast Asia. Over the period from 1966–1996, the annual water discharge and sediment load at Pyay station were estimated to be 332–379 km^3 and 268–382 Mt respectively (Furuichi et al., 2009). The IRD has a catchment area of 404,100 km^2, a population of 11 million, and a mean tidal range of approximately 2.7 m in its estuary. Fourteen dams are in operation and several embankments have been built along the Irrawaddy River. Green forest and crop cultivation cover more than 60% of the basin area. Therefore, compared with the PRD, the IRD can be considered as a nearly natural system with only limited human activity (Garzanti et al., 2016).

3. Data and methods

The methodological framework used in this paper involves four main steps (Fig. 2): (1) the development of an automatic water extraction and water occurrence algorithm to generate a water body mask (Section 3.2); (2) the delineation of raster and vector DCNs through the application of morphological algorithms (Section 3.3); (3) the calculation of channel widths and the quantification of their variations and migration based on the Digital Shoreline Analysis System (Section 3.4); (4) an assessment of the mapping accuracy and analysis of the uncertainty of our methodological framework (Section 3.5).

3.1. Data collection

3.1.1 Satellite data

With a 30-m resolution and 16-day repeat cycle, Landsat archives, including the Landsat 5 Thematic Mapper (TM), the Landsat 7 Enhanced Thematic Mapper-plus (ETM+), and the Landsat 8 Operational Land Imager (OLI), provide a spatially and temporally consistent resolution at the global scale (Claverie et al., 2015; Irons et al., 2012). In this study, we created three-year temporal-scale water occurrence composite imagery for both deltas from Landsat data covering four periods, including 1986-1988, 1996-1998, 2006-2008, and 2016-2018. We did so in order to minimize the effects of cloud cover and hydrological extremes. Our analysis used a total of 2,307 Landsat surface reflectance images georeferenced with high accuracy (<0.4 pixels; Table 1). The Quality Assessment (QA) band of each Landsat image was generated by the CFMask algorithm, which identified pixels that exhibited adverse instrumentational, atmospheric, or surface conditions, and which subsequently removed poor-quality observations (e.g., cloud, cloud shadows, etc.) (Foga et al., 2017). All the Landsat images were collected and computed on the cloud-based Google Earth Engine (GEE) platform (Gorelick et al., 2017). In addition, we collected five high-resolution images (i.e., Pleiades-1A and WorldView-2; Table 2) from the period between 2016-2018 with 0.5-m spatial resolution as reference data for accuracy assessment.

3.1.2 Gauging station data

We collected the annual water discharge and sediment load at gauging stations (i.e., the Boluo, Gaoyao and Shijiao stations) in the upper basin of the Pearl River from 1954 to 2018. The annual water level data at four gauging stations (the Hengmen, Baijiao, Huangjin and Hengshan stations) near the river outlets from 1986 to 2017 was also captured. These datasets originate from the Hydrologic Yearbooks issued by the Ministry of Water Resources of China. Because of the difficulty of obtaining reliable hydrological data in the Irrawaddy River basin, we were only able to access annual water and sediment discharge data from the Pyay station between 1966–1996 and the Magway station between 1990–2010 from previously published research (Furuichi et al., 2009; Lazarus et al., 2019). The locations of these gauging stations are shown in Figs.1a-b.

3.2. Water occurrence algorithm with Landsat time series

A series of spectral and water indices, such as the NDWI, MNDWI, and AWEI, have been used for water classification and extraction (Alsdorf et al., 2007; Mueller et al., 2016). The MNDWI can achieve more than 98% accuracy in identifying water pixels based on the Landsat archive of images from the TM, ETM+, and OLI sensors (Feyisa et al., 2014; Fisher et al., 2016). We calculated the MNDWI using surface reflectance data from the green and first shortwave infrared (SWIR1) bands of every Landsat image in the image collection after applying the cloud mask. The MNDWI at time t is defined by the equation:

$$\mathrm{MNDWI}_t = (\rho_{Green,t} - \rho_{SWIR1,t})/(\rho_{Green,t} + \rho_{SWIR1,t}) \quad (1)$$

where $\rho_{Green,t}$ is the surface reflectance of the green band at time t and $\rho_{SWIR,t}$ is the surface reflectance of the SWIR1 band at time t. Otsu's (1979) thresholding method was then adopted to automatically distinguish between water and non-water pixels from all MNDWI values for each scene. Due to water runoff, tidal effects, and rainfall in river deltas, fluctuations in water levels occur continually in DCNs. For each pixel, the water occurrence frequency can be defined as the ratio between the number of measurements that classify a pixel as water and the total number of measurements in a time-series MNDWI stacking. This is expressed as:

$$P_{water} = n_{water}/N \quad (2)$$

where P_{water} is the relative frequency of water occurrence, n_{water} is the number of measurements that are classified as water at the pixel location, and N is the total number of measurements at the pixel location. The water body mask was determined using the given

P_{water} threshold. High P_{water} values represent permanent water bodies, and the low P_{water} values show temporary water bodies (i.e., paddy fields, inundation areas and tidal wetlands), as well as potential regions that are affected by extreme water level fluctuations (Fig. 3b, light blue areas). The P_{water} threshold was determined as 0.5 in order to mitigate these uncertain effects. That is, a pixel was classified as water if its P_{water} value was greater than or equal to 0.5; otherwise, the pixel was classified as non-water (Fig. 3c).

3.3. Spatial morphological delineation of channel networks

In order to accurately delineate the centerlines and banklines of the channel network, we removed small channel bars or river islands with areas less than 1 km^2 (about the size of 1100 pixels in the Landsat imagery) and bodies of water that were not connected with a channel network (such as reservoirs, aquaculture ponds, and wetlands). Doing so also allowed us to avoid spatial shifts or displacements of the centerline position for the main channel. The gaps caused by bridges over channels were filled manually to ensure complete connectivity of the channel network. The “Clump” morphological operation was used to group adjacent water pixels to regions and the “Sieve” operation was performed to remove regions with areas smaller than a user-specified size (Fig. 3c). The centerlines and banklines of the channels were delineated from binary images using two morphological vectorization methods, “centerline” and “outline,” which were implemented in ArcScan, an extension tool in ArcGIS 10.5. The centerline vectorization method can generate vector features along the center of the raster linear elements and was used to build the centerline elements for the channels. The centerlines were split up into multiple elements when bifurcations occurred. The outline vectorization method generates vector features at the border of raster linear elements and was used to delineate the channel banklines (Fig. 3d).

3.4. Change analysis of DCNs

In order to quantify changes in DCNs, the Digital Shoreline Analysis System (DSAS) (Himmelstoss et al., 2018), which was developed by the USGS to compute rate-of-change statistics for time series shoreline vector data, was employed to calculate the channel width throughout the 1986–2018 period at 10-year intervals. We constructed the baseline series for four periods based on the DCN centerlines and cast transect lines perpendicular to the baseline at 100 m intervals. All of the transects intersected with multi-temporal banklines were used to establish measurement points for the rate calculations. The channel width was calculated as the sum of the distances from the measurement points to the baseline, and the channel migration was calculated as the displacement among the centerlines (Fig. 3e-f). Three rate-of-change statistical methods in DSAS were used to assess changes in the channel. These are: the Net Shoreline Movement (NSM), which is calculated as the distance between the oldest and most recent banklines for each transect; the End Point Rate (EPR), which is calculated by dividing the shoreline movement by the time elapsed between the oldest and the most recent banklines; and the Linear Regression Rate (LRR), which is calculated by fitting a least-squares regression line to all shoreline points for a transect.

3.5. Accuracy assessment and sensitivity analysis

The uncertainty of our methodological framework may have resulted from water extraction based on single images using Otsu's thresholding and the determination of the boundaries of rivers from time-series MNDWI images using the water occurrence algorithm. The “Clump” and “Sieve” morphological operations were not expected to introduce additional uncertainties as they only acted on surface waters disconnected to channel networks. To assess the uncertainty resulting from Otsu’s thresholding method, we manually digitized river polygons based on a Pleiades-1A satellite image captured on November 23, 2018 and compared those with the river polygons derived from one Landsat image at the closest time acquired on November 24, 2018. We then performed a pixel-by-pixel assessment of water extraction accuracy based on the following three metrics: the overall accuracy (OA), the user’s accuracy (UA), and producer’s accuracy (PA). Considering the water level fluctuations caused by seasonal precipitation variations between wet and dry seasons, we also manually digitized the “true” boundaries of validated rivers from four reference images acquired in the wet and dry seasons. The channel width error was calculated as the difference between the extracted channel widths derived from 0.5 water occurrence and the validated channel widths calculated according to the reference boundaries. The root-mean-square error (RMSE) was also computed to assess the accuracy of our measurements. Furthermore, to evaluate the sensitivity of our determination based on the 0.5 water occurrence threshold, we also calculated and compared channel widths using a wide range of thresholds (0.1, 0.3, 0.7, and 0.9) for water occurrence.

4. Results

4.1. Channel width and its variations

The results in Fig. 4a and 4b were derived from 1986–2018 Landsat time series and show that the average channel widths of the PRD and IRD are 387.6 m and 300.9 m respectively, and the maximum channel widths are 4261 m and 7723 m, respectively. The associated total river mouth widths for the PRD and IRD are 13.2 km (eight river outlets) and 36.84 km (twelve river outlets), respectively. Fig. 4a shows that the eight outlets of the PRD have mean channel widths ranging from 335–2054 m. In performing a Kruskal-Wallis one-way analysis of variance by ranks at the confidence level of 95%, we found that seven of these outlets have undergone significant shrinkage over the past 33 years, with average shrinkage rates varying from 1.0–5.4 m/year. By contrast, Fig. 4b shows that the mean outlet widths of the IRD, ranging from 295–4784 m, have remained largely stable. Only one outlet (No. 8) has undergone significant shrinkage, with average shrinkage rates of 1.9 m/year. Two of the outlets (No. 11 and 12) have expanded, with average expansion rates of 1.2–2.5 m/year, these changes, however, not statistically significant. The other outlets in the IRD display no significant change, with average change rates varying from −0.5 to 0.6 m/year. The PRD and IRD have different change patterns in their estuarine systems. Most of outlets in the PRD have shrunk with average rates of 0.4–6.4 m/year, while most of the IRD outlets have remained stable.

We analyzed in detail the width variations in the three main distributary channels of the PRD (West River, North River, and East River) (Fig. 1a, Fig. 5a–c) and the six main distributary channels of the IRD (Pathein River, Ywe River, Pyamalaw River, Irrawaddy River, Toe River, and Yangon River) (Fig. 1b, Fig. 5d–i) over 33 years (1986–2018). The results attained for the PRD, illustrated in Fig. 5, show obvious channel shrinkages in the estuarine sections of the East River and North River (within 30 km distance from the mouth), but only minor changes in the West River. In the IRD, six of the main distributary channels display a similar pattern in which changes in the channel width were more significant in the estuarine regions than in the upstream regions. The Pyamalaw River, Irrawaddy River, Toe River, and Yangon River exhibit evident expansion in their estuarine regions, while slight channel shrinkage can be seen in some sections of the Pathein River and Yway River.

4.2. Channel migration

There are evident spatial differences in channel migrations for both deltas and, specifically, channels shifted more rapidly in the IRD than they did in the PRD. Major channel migrations were observed in the upper sections of both deltas, though there was very little channel migration visible in either the Pearl River or Irrawaddy River estuarine areas (within 30 km distance from the mouth). However, due to geomorphological evolution (i.e., the erosion or accumulation of mid-channel bars), some channel segments in the estuarine areas of the PRD and IRD also experienced slight migrations, with migration rates of 0.1-0.4 m/year and 0.5-1.1 m/year, respectively. In the upper section of the North River (~100 km distance from the mouth) in the PRD, the channel migrated with a mean migration rate of 1.2 m/year. Large-scale channel migrations (~15 m/year) were observed in the upper section of the Irrawaddy River (~130 km distance from the mouth). A closer investigation of channel migration patterns over time revealed that two patterns of channel migration could be identified: regular and random (Fig. 6). Regular migration is defined as a channel gradually shifting in the same direction, and this form of migration can be quantified, simulated, and predicted. Random migration is defined as a varying migratory direction over time induced by the combined geomorphological evolution of channel bars and banks, which is potentially more difficult to predict through modeling.

4.3. Validation

To quantify the accuracy of our channel extraction method, we focused on Otsu's method and the influence of the chosen 0.5 water occurrence threshold. Otsu's thresholding method for classifying water pixels resulted in 98.8% overall accuracy (OA), 98.1% producer's accuracy (PA) and 98.6% user's accuracy (UA). Errors of commission and omission mainly occurred at the river boundaries, where bodies of water consisted of mixed pixels, which was evident when the binary classifications were visually compared to the river boundaries delineated from the high-resolution reference images (Fig. 7a-b). These errors may have led to either the overestimation or underestimation of channel widths. In order to assess the overall accuracy of channel width estimation, a total of 892 records of channel widths were calculated. Fig. 7c shows a histogram and the cumulative probability distribution of channel width errors, where more than 94% of width errors were within a single Landsat pixel (i.e., 30 m), with a RMSE of 15.1 m. Analysis of the relationship between channel widths calculated from 0.5 water occurrence images and extracted from reference images acquired during both dry and wet seasons gave an R^2 of 0.98. This demonstrates that our approach maintains a high degree of accuracy in both the dry and wet seasons, and in comparison with the channel widths derived from other water occurrence images (Fig. 8). Lower water occurrence (i.e., 0.1, Fig. 8b) may result in the overestimation of channel widths while higher water occurrence (i.e., 0.9, Fig. 8f) may lead to their underestimation. Therefore, channel widths derived from the 0.5 water occurrence can better represent temporal variability in river widths (e.g., seasonal precipitation variations) and they are more suitable for tracking the deltaic channel dynamics.

5. Discussion

5.1. Drivers of channel evolution

Previous studies have suggested that the evolution of the DCNs to be mainly driven by alterations in water discharge and sediment load in the basin, which has resulted from climate change, reservoir/dam constructions, and land use change (Lu et al., 2007; Nelson et al., 2015; Syvitski et al., 2005). Relationships between water discharge and precipitation may be an indication that annual water discharge has been strongly influenced by climate change (Wu et al., 2012). However, the assessment of the climatic impact on sediment load is challenging due to other potential anthropogenic factors. In the PRD, more than 90 dams and reservoirs (>0.1 km^3 storage capacity) have been constructed in the Pearl River basin since the 1980s with a total reservoir storage capacity totaling 65 km^3. Fig. 9a shows that, prior to widespread dam construction, the annual sediment and water discharges from the Pearl River were approximately 80–85 Mt and 280–285 km^3, respectively. Since 1994, the annual sediment discharge declined from about 129 Mt to a minimum of 15 Mt in 2007. Since 2007, due to the closure of the Longtan Dam (second in size only to the Three Gorges Dam), the annual sediment and water discharges have averaged around 23 Mt and 275 km^3, respectively, with standard deviations of ±10 Mt and ±55 km^3, respectively. These river dams are capable of changing the flow patterns especially on a seasonal scale and they reduce the sediment load of the rivers, which alters the sediment transport capacity and geomorphological development of the channel network system. The full geomorphic impacts of hydropower projects can take years or even decades to unfold, mostly due to the large volumes of sediment stored in the downstream river channels that can buffer their impacts for extended periods (Yang et al., 2011). Our analysis, which considers both human and natural factors, shows that the channel width has shrunk since 1986 and that this trend has been significantly enhanced by human disturbance.

In contrast with the Pearl River basin, dam construction in the Irrawaddy River basin is relatively low with only 14 hydropower stations being built, with 3 under construction, 29 having been proposed, and 2 having been suspended (Lazarus et al., 2018). We collected the available annual water and sediment discharge data from Pyay station between 1966–1996 and the Magway station between 1990–2010. As seen in Fig. 9b, the hydrological conditions remained relatively stable over these periods with a higher discharge compared to the Pearl River. Much of the DCNs in the IRD are prone to channel changes and migration as the river is unconstrained and has relatively low slopes with high sediment loads. Runoff with high flow velocities accelerates erosion on one side of the channel and deposits sediment on the other, which gradually leads to regular channel migration (as seen in Fig. 6a). Therefore, the potential impacts of dam construction on the channel network system in the IRD should be monitored in the future.

The evaluation of the impacts of other forms of human activity and the measurement of their influence on channel changes is difficult, since it requires more long-term integrated observations and high-accuracy process-based modeling (Nahon et al., 2012; Wei and Wu, 2014). It is known that vegetation degradation and terrestrial mining generally increase the sediment inputs into river systems and alter rainwater runoff. The IRD has rich mineral resources, especially gold and jade, and mining activities would likely result in larger sediment particle input into its rivers. This could influence the transport of suspended and bedload sediment in the river system. An additional anthropogenic impact on channel evolution in the PRD and IRD is from in-channel sand mining. It has been estimated that approximately 60–69 Mt/year of riverbed sediment is extracted from the Pearl River (Wu et al., 2014), and approximately 20 Mt/year of sediment, or 10% of the total sediment load, is excavated from the Irrawaddy River (Chen et al., 2020a). This has likely caused different levels of bank erosion than shown by our results due to the reduced friction and increased water velocity after sand removal. In addition, riparian tideland reclamation for urban development in the Pearl River estuarine regions also accounts for the major shrinkage of channels.

5.2. Implications for river management

Large rivers and their floodplains support huge populations globally and provide diverse ecosystems. However, these rivers have changed in morphology through time due to a combination of anthropogenic interventions and climate change (Best, 2018) The maintenance of bank stability and channel capacity are crucially important for flooding prevention and navigation safety. Therefore, many local or regional policies, such as the Lancang-Mekong Cooperation Mechanism (LMC) (Feng et al., 2019), were established to create and manage sustainable development goals within river ecosystems. In this study, our results indicate that channel width changes and channel migrations have huge spatial variations. Based on the results provided by our study, it would be possible to identify highly dynamic segments of rivers and delta channels and to establish a link between changes in delta network patterns and sediment delivery. This information would be crucial for the creation of goal-oriented management plans, such as in defining thresholds for sediment and discharge levels in order to maintain network states at certain distances from the mouth. Rapid channel narrowing in the estuarine areas of the PRD (within 30 km distance from the mouth) was largely caused by riparian tideland reclamation, which has the effect of decreasing the cross-sectional flow area and increasing the potential for flooding in urban areas in the context of rising sea levels (Fig. 10). This has the potential to aggravate the threat of urban waterlogging and saline water intrusion in the future. Consequently, the ground covers for wetlands on the fringes of DCNs should be preserved in order to create a sufficient buffer for peak river discharge levels and also to preserve valuable ecosystem, which are essential for maintaining economic resources such as fisheries. Furthermore, our methodological framework for quantifying channel changes can support decision-making processes for local and global river management activities in the future.

5.3. Limitations

Our methodological framework is hindered by the uncertainty of the delineation of river networks stemming from the limited spatial resolution of Landsat images (30 m per pixel), which inevitably leads to ambiguities in the determination of river boundaries. The presence of mixed pixels at channel boundaries may result in either the overestimation or underestimation of channel widths. Compared with previous approaches (Chen et al., 2020b; Isikdogan et al., 2017; Monegaglia et al., 2018), our method performs better for small channels. Channels with a width close to or narrower than the resolution of the input images can be delineated with an improved accuracy. This is due to the fact that the extraction of such small channels from single image could lead to ambiguous results (Fig. 11a). The analysis of these kinds of small channels, however, can be enhanced by time-series observations (Fig. 11b-c). As images generated by sensors with finer spatial resolution have begun to become freely available in recent years, for example, the Sentinel-1 and Sentinel-2 missions (10 m per pixel and six-day revisit), it will be possible to quantify changes in DCNs at a fine spatial resolution and high temporal frequency in the future (Fig. 11d). In addition, previous studies have attempted to increase the mapping accuracy of Landsat images to subpixel levels using spectral unmixing (Sun et al., 2017; Xie et al., 2016) and subpixel localization algorithms (Bishop-Taylor et al., 2019; Song et al., 2019). While these techniques perform generally well in certain situations, challenges remain in terms of endmember sample selection, consistency of subpixel localization accuracy, and large-scale automation for generalization, making the production of seamless and consistent datasets through time and across complex and dynamic heterogeneous environments arduous (Bishop-Taylor et al., 2019).

Another limitation is the lack of depth measurements in terms of the characterization of channel geomorphology using time-series of Landsat remote sensing images. We used the centerline changes to indicate channel migrations—an approach that only documents the horizontal (i.e., platform) dimension. However, changes in channel depth, such as movement of the thalweg, might be more representative for the response of river systems to various disturbances (Liu et al., 2019). Even so, there are some obstacles to obtaining *in-situ* bathymetric data, such as the high cost and the amount of time required to collect such data at local scales. Satellite-derived river bathymetry algorithms have been developed in the recent research, those using including spectrally-based methods (Legleiter and Harrison, 2019; Niroumand-Jadidi et al., 2020) and hydraulic relationships-based models (Breda et al., 2019; Moramarco et al., 2019). These spectrally-based techniques have been demonstrated to be effective in clear and shallow water bodies where the spectral signal is dominated by bottom reflected radiation (Kasvi et al., 2019; Niroumand-Jadidi et al., 2018). The direct retrieval of bathymetry, however, is quite challenging under conditions of high turbidity in DCNs as the result of the flow of upstream sediment, organic matter, and other materials. The hydraulic relationships-based models commonly need precise channel width as their input (Schaperow et al., 2019). Thus, the channel widths calculated from our method can provide an accurate and robust channel width dataset in order to enhance river depth estimation based on the hydraulic relationships. These are the programme of research we would like to pursue in the future.

6. Conclusion

This study proposes a quantitative framework to map and analyze the long-term evolution of DCNs. After applying our framework to two case studies, we found that most of the channels in the PRD underwent significant shrinkage, whereas only slight changes were observed in the IRD. These results indicate that human interventions have greatly altered deltaic channel morphology by impacting sediment load in the river basin. In terms of channel mobility, significant channel migrations occurred in the meandering regions of the IRD, while other channel shifts were not as obvious. Very little migration was observed in the channel network of the PRD. These stepwise adjustments in the DCNs may lead to the redistribution of water and sediment discharges, which can affect the patterns of the deltaic system evolution. This is an important issue for river deltas and should be addressed in future work. The methodological framework proposed in this study provides a practical and effective way to monitor deltaic channel evolution and could be used to develop a new global hydrological product, as well as improving the study of hydrological processes and the future sustainable management of global river ecosystems.

Declaration of interests

The authors declare that they have no known competing financial interests or personal relationships that could have appeared to influence the work reported in this paper.

Acknowledgments

Funding: This work was supported by a grant from the National Key Research and Development Program of China [grant number 2018YFE0101000], the National Nature Science Foundation of China [grant number 51739005] and the project "Coping with deltas in transition" within the Programme of Strategic Scientific Alliances between China and the Netherlands (PSA), financed by the Ministry of Science and Technology of the People's Republic of China (MOST) [grant number 2016YFE0133700].

Reference

Abed-Elmdoust, A., Miri, M.-A., Singh, A., 2016. Reorganization of river networks under changing spatiotemporal precipitation patterns: An optimal channel network approach. Water Resources Research, 52(11): 8845-8860. DOI:10.1002/2015wr018391

Alsdorf, D.E., Rodriguez, E., Lettenmaier, D.P., 2007. Measuring surface water from space. Reviews of Geophysics, 45(2). DOI:Artn Rg200210.1029/2006rg000197

Best, J., 2018. Anthropogenic stresses on the world's big rivers. Nat Geosci, 12(1): 7-21. DOI:10.1038/s41561-018-0262-x

Bishop-Taylor, R., Sagar, S., Lymburner, L., Alam, I., Sixsmith, J., 2019. Sub-Pixel Waterline Extraction: Characterising Accuracy and Sensitivity to Indices and Spectra. Remote Sensing, 11(24). DOI:ARTN 298410.3390/rs11242984

Breda, J.P.L.F., Paiva, R.C.D., Bravo, J.M., Passaia, O.A., Moreira, D.M., 2019. Assimilation of Satellite Altimetry Data for Effective River Bathymetry. Water Resources Research, 55(9): 7441-7463. DOI:10.1029/2018wr024010

Chen, D. et al., 2020a. Recent evolution of the Irrawaddy (Ayeyarwady) Delta and the impacts of anthropogenic activities: A review and remote sensing survey. Geomorphology, 365. DOI:ARTN 10723110.1016/j.geomorph.2020.107231

Chen, H.L., Liang, Q.H., Liang, Z.Y., Liu, Y., Ren, T.Y., 2020b. Extraction of connected river networks from multi-temporal remote sensing imagery using a path tracking technique. Remote Sensing of Environment, 246. DOI:ARTN11186810.1016/j.rse.2020.111868

Claverie, M., Vermote, E.F., Franch, B., Masek, J.G., 2015. Evaluation of the Landsat-5 TM and Landsat-7 ETM+ surface reflectance products. Remote Sensing of Environment, 169: 390-403. DOI:10.1016/j.rse.2015.08.030

Feng, Y., Wang, W., Suman, D., Yu, S., He, D., 2019. Water Cooperation Priorities in the Lancang-Mekong River Basin Based on Cooperative Events Since the Mekong River Commission Establishment. Chinese Geographical Science, 29(1): 58-69. DOI:10.1007/s11769-019-1016-4

Feyisa, G.L., Meilby, H., Fensholt, R., Proud, S.R., 2014. Automated Water Extraction Index: A new technique for surface water mapping using Landsat imagery. Remote Sensing of Environment, 140: 23-35. DOI:10.1016/j.rse.2013.08.029

Fisher, A., Flood, N., Danaher, T., 2016. Comparing Landsat water index methods for automated water classification in eastern Australia. Remote Sensing of Environment, 175: 167-182. DOI:10.1016/j.rse.2015.12.055

Foga, S. et al., 2017. Cloud detection algorithm comparison and validation for operational Landsat data products. Remote Sensing of Environment, 194: 379-390. DOI:10.1016/j.rse.2017.03.026

Furuichi, T., Win, Z., Wasson, R.J., 2009. Discharge and suspended sediment transport in the Ayeyarwady River, Myanmar: centennial and decadal changes. Hydrological Processes, 23(11): 1631-1641. DOI:10.1002/hyp.7295

Garzanti, E., Wang, J.-G., Vezzoli, G., Limonta, M., 2016. Tracing provenance and sediment fluxes in the Irrawaddy River basin (Myanmar). Chemical Geology, 440: 73-90. DOI:10.1016/j.chemgeo.2016.06.010

Gong, Z.N. et al., 2020. Extracting tidal creek features in a heterogeneous background using Sentinel-2 imagery: a case study in the Yellow River Delta, China. Int J Remote Sens, 41(10): 3653-3676. DOI:10.1080/01431161.2019.1707898

Gorelick, N. et al., 2017. Google Earth Engine: Planetary-scale geospatial analysis for everyone. Remote Sensing of Environment, 202: 18-27. DOI:10.1016/j.rse.2017.06.031

Gugliotta, M., Saito, Y., 2019. Matching trends in channel width, sinuosity, and depth along the fluvial to marine transition zone of tide-dominated river deltas: The need for a revision of depositional and hydraulic models. Earth-Sci Rev, 191: 93-113. DOI:10.1016/j.earscirev.2019.02.002

Himmelstoss, E.A., Henderson, R.E., Kratzmann, M.G., Farris, A.S., 2018. Digital Shoreline Analysis System (DSAS) version 5.0 user guide. 2331-1258, US Geological Survey. DOI:10.3133/ofr20181179

Irons, J.R., Dwyer, J.L., Barsi, J.A., 2012. The next Landsat satellite: The Landsat Data Continuity Mission. Remote Sensing of Environment, 122: 11-21. DOI:10.1016/j.rse.2011.08.026

Isikdogan, F., Bovik, A., Passalacqua, P., 2015. Automatic Channel Network Extraction From Remotely Sensed Images by Singularity Analysis. IEEE Geoscience and Remote Sensing Letters, 12(11): 2218-2221. DOI:10.1109/lgrs.2015.2458898

Isikdogan, F., Bovik, A., Passalacqua, P., 2017. RivaMap: An automated river analysis and mapping engine. Remote Sensing of Environment, 202: 88-97. DOI:10.1016/j.rse.2017.03.044

Jarriel, T., Isikdogan, L.F., Bovik, A., Passalacqua, P., 2019. Characterization of Deltaic Channel Morphodynamics From Imagery Time Series Using the Channelized Response Variance. Journal of Geophysical Research: Earth Surface, 124(12): 3022-3042. DOI:10.1029/2019jf005118

Kasvi, E., Salmela, J., Lotsari, E., Kumpula, T., Lane, S., 2019. Comparison of remote sensing based approaches for mapping bathymetry of shallow, clear water rivers. Geomorphology, 333: 180-197. DOI:10.1016/j.geomorph.2019.02.017

Klemenjak, S., Waske, B., Valero, S., Chanussot, J., 2012. Automatic Detection of Rivers in High-Resolution SAR Data. Ieee J-Stars, 5(5): 1364-1372. DOI:10.1109/jstars.2012.2189099

Kulp, S.A., Strauss, B.H., 2019. New elevation data triple estimates of global vulnerability to sea-level rise and coastal flooding. Nat Commun, 10(1): 4844. DOI:10.1038/s41467-019-12808-z

Lazarus, K.M., Cardinale, P., Corbett, M., Lin, N.S., Noeske, T.K.H., 2019. Baseline Assessment Report: Geomorphic and Sediment Transport, The World Bank.

Lazarus, K.M., Corbett, M., Cardinale, P., Lin, N.S., Noeske, T.K.H., 2018. Strategic Environmental Assessment of the Myanmar Hydropower Sector: Final Report, World Bank Group, Washington, D.C.

Lee, H., Chae, H., Cho, S.-J., 2011. Radar Backscattering of Intertidal Mudflats Observed by Radarsat-1 SAR Images and Ground-Based Scatterometer Experiments. IEEE Trans. Geosci. Remote Sensing, 49(5): 1701-1711. DOI:10.1109/tgrs.2010.2084094

Legleiter, C.J., Harrison, L.R., 2019. Remote Sensing of River Bathymetry: Evaluating a Range of Sensors, Platforms, and Algorithms on the Upper Sacramento River, California, USA. Water Resources Research, 55(3): 2142-2169. DOI:10.1029/2018wr023586

Li, X., Lyu, X., Tong, Y., Li, S.Y., Liu, D.F., 2019. An Object-Based River Extraction Method via Optimized Transductive Support Vector Machine for Multi-Spectral Remote-Sensing Images. Ieee Access, 7: 46165-46175. DOI:10.1109/Access.2019.2908232

Liu, F. et al., 2019. Stepwise adjustment of deltaic channels in response to human interventions and its hydrological implications for sustainable water managements in the Pearl River Delta, China. Journal of Hydrology, 573: 194-206. DOI:10.1016/j.jhydrol.2019.03.063

Lu, X.X., Zhang, S.R., Xie, S.P., Ma, P.K., 2007. Rapid channel incision of the lower Pearl River (China) since the 1990s as a consequence of sediment depletion. Hydrol Earth Syst Sc, 11(6): 1897-1906. DOI:10.5194/hess-11-1897-2007

McFeeters, S.K., 1996. The use of the Normalized Difference Water Index (NDWI) in the delineation of open water features. Int J Remote Sens, 17(7): 1425-1432. DOI:10.1080/01431169608948714

Mei, X. et al., 2018. Secular bathymetric variations of the North Channel in the Changjiang (Yangtze) Estuary, China, 1880–2013: Causes and effects. Geomorphology, 303: 30-40. DOI:10.1016/j.geomorph.2017.11.014

Monegaglia, F., Zolezzi, G., Güneralp, I., Henshaw, A.J., Tubino, M., 2018. Automated extraction of meandering river morphodynamics from multitemporal remotely sensed data. Environmental Modelling & Software, 105: 171-186. DOI:10.1016/j.envsoft.2018.03.028

Moramarco, T., Barbetta, S., Bjerklie, D.M., Fulton, J.W., Tarpanelli, A., 2019. River Bathymetry Estimate and Discharge Assessment from Remote Sensing. Water Resources Research, 55(8): 6692-6711. DOI:10.1029/2018wr024220

Mueller, N. et al., 2016. Water observations from space: Mapping surface water from 25 years of Landsat imagery across Australia. Remote Sensing of Environment, 174: 341-352. DOI:10.1016/j.rse.2015.11.003

Nahon, A., Bertin, X., Fortunato, A.B., Oliveira, A., 2012. Process-based 2DH morphodynamic modeling of tidal inlets: A comparison with empirical classifications and theories. Marine Geology, 291: 1-11. DOI:10.1016/j.margeo.2011.10.001

Nelson, P.A., Brew, A.K., Morgan, J.A., 2015. Morphodynamic response of a variable‐width channel to changes in sediment supply. Water Resources Research, 51(7): 5717-5734. DOI:10.1002/2014wr016806

Niroumand-Jadidi, M., Bovolo, F., Bruzzone, L., 2020. SMART-SDB: Sample-specific multiple band ratio technique for satellite- derived bathymetry. Remote Sensing of Environment, 251. DOI:ARTN 112091
10.1016/j.rse.2020.112091

Niroumand-Jadidi, M., Vitti, A., Lyzenga, D.R., 2018. Multiple Optimal Depth Predictors Analysis (MODPA) for river bathymetry: Findings from spectroradiometry, simulations, and satellite imagery. Remote Sensing of Environment, 218: 132-147. DOI:10.1016/j.rse.2018.09.022

Obida, C.B., Blackburn, G.A., Whyatt, J.D., Semple, K.T., 2019. River network delineation from Sentinel-1 SAR data. Int J Appl Earth Obs, 83. DOI:10.1016/j.jag.2019.101910

Otsu, N., 1979. A threshold selection method from gray-level histograms. IEEE transactions on systems, man, and cybernetics, 9(1): 62-66. DOI:10.1109/TSMC.1979.4310076

Passalacqua, P., Do Trung, T., Foufoula-Georgiou, E., Sapiro, G., Dietrich, W.E., 2010. A geometric framework for channel network extraction from lidar: Nonlinear diffusion and geodesic paths. Journal of Geophysical Research, 115(F1). DOI:10.1029/2009jf001254

Pavelsky, T.M., Smith, L.C., 2008. RivWidth: A Software Tool for the Calculation of River Widths From Remotely Sensed Imagery. IEEE Geoscience and Remote Sensing Letters, 5(1): 70-73. DOI:10.1109/lgrs.2007.908305

Rahmstorf, S., 2017. Rising hazard of storm-surge flooding. Proc Natl Acad Sci U S A, 114(45): 11806-11808. DOI:10.1073/pnas.1715895114

Remo, J.W.F., Ickes, B.S., Ryherd, J.K., Guida, R.J., Therrell, M.D., 2018. Assessing the impacts of dams and levees on the hydrologic record of the Middle and Lower Mississippi River, USA. Geomorphology, 313: 88-100. DOI:10.1016/j.geomorph.2018.01.004

Rowland, J.C. et al., 2016. A morphology independent methodology for quantifying planview river change and characteristics from remotely sensed imagery. Remote Sensing of Environment, 184: 212-228. DOI:10.1016/j.rse.2016.07.005

Schaperow, J.R., Li, D.Y., Margulis, S.A., Lettenmaier, D.P., 2019. A Curve-Fitting Method for Estimating Bathymetry From Water Surface Height and Width. Water Resources Research, 55(5): 4288-4303. DOI:10.1029/2019wr024938

Schwenk, J., Khandelwal, A., Fratkin, M., Kumar, V., Foufoula-Georgiou, E., 2017. High spatiotemporal resolution of river planform dynamics from Landsat: The RivMAP toolbox and results from the Ucayali River. Earth Space Sci, 4(2): 46-75. DOI:10.1002/2016ea000196

Shahrood, A.J. et al., 2020. RiMARS: An automated river morphodynamics analysis method based on remote sensing multispectral datasets. Science of the Total Environment, 719. DOI:ARTN 13733610.1016/j.scitotenv.2020.137336

Sirisena, T.A.J.G., Maskey, S., Ranasinghe, R., Babel, M.S., 2018. Effects of different precipitation inputs on streamflow simulation in the Irrawaddy River Basin, Myanmar. Journal of Hydrology: Regional Studies, 19: 265-278. DOI:10.1016/j.ejrh.2018.10.005

Song, Y., Liu, F., Ling, F., Yue, L.W., 2019. Automatic Semi-Global Artificial Shoreline Subpixel Localization Algorithm for Landsat Imagery. Remote Sensing, 11(15). DOI:10.3390/rs11151779

Sun, W., Du, B., Xiong, S., 2017. Quantifying Sub-Pixel Surface Water Coverage in Urban Environments Using Low-Albedo Fraction from Landsat Imagery. Remote Sensing, 9(5). DOI:10.3390/rs9050428

Syvitski, J.P.M., Kettner, A.J., Correggiari, A., Nelson, B.W., 2005. Distributary channels and their impact on sediment dispersal. Marine Geology, 222-223: 75-94. DOI:10.1016/j.margeo.2005.06.030

Syvitski, J.P.M. et al., 2009. Sinking deltas due to human activities. Nat Geosci, 2(10): 681-686. DOI:10.1038/ngeo629

Wang, B., Xu, Y.J., 2018. Dynamics of 30 large channel bars in the Lower Mississippi River in response to river engineering from 1985 to 2015. Geomorphology, 300: 31-44. DOI:10.1016/j.geomorph.2017.09.041

Wei, X., Wu, C.Y., 2014. Long-term process-based morphodynamic modeling of the Pearl River Delta. Ocean Dynam, 64(12): 1753-1765. DOI:10.1007/s10236-014-0785-7

Willett, S.D., McCoy, S.W., Perron, J.T., Goren, L., Chen, C.Y., 2014. Dynamic reorganization of river basins. Science, 343(6175): 1248765. DOI:10.1126/science.1248765

Wu, C.S., Yang, S.L., Lei, Y.-p., 2012. Quantifying the anthropogenic and climatic impacts on water discharge and sediment load in the Pearl River (Zhujiang), China (1954–2009). Journal of Hydrology, 452-453: 190-204. DOI:10.1016/j.jhydrol.2012.05.064

Wu, Z. et al., 2018. Geomorphologic changes in the lower Pearl River Delta, 1850–2015, largely due to human activity. Geomorphology, 314: 42-54. DOI:10.1016/j.geomorph.2018.05.001

Wu, Z.Y., Milliman, J.D., Zhao, D.N., Zhou, J.Q., Yao, C.H., 2014. Recent geomorphic change in LingDing Bay, China, in response to economic and urban growth on the Pearl River Delta, Southern China. Global and Planetary Change, 123: 1-12. DOI:10.1016/j.gloplacha.2014.10.009

Xie, H., Luo, X., Xu, X., Pan, H., Tong, X., 2016. Automated Subpixel Surface Water Mapping from Heterogeneous Urban Environments Using Landsat 8 OLI Imagery. Remote Sensing, 8(7). DOI:10.3390/rs8070584

Xu, H., 2006. Modification of normalised difference water index (NDWI) to enhance open water features in remotely sensed imagery. Int J Remote Sens, 27(14): 3025-3033. DOI:10.1080/01431160600589179

Yamazaki, D. et al., 2014. Development of the Global Width Database for Large Rivers. Water Resources Research, 50(4): 3467-3480. DOI:10.1002/2013wr014664

Yang, K. et al., 2014. River Delineation from Remotely Sensed Imagery Using a Multi-Scale Classification Approach. Ieee J-Stars, 7(12): 4726-4737. DOI:10.1109/jstars.2014.2309707

Yang, K. et al., 2015. River Detection in Remotely Sensed Imagery Using Gabor Filtering and Path Opening. Remote Sensing, 7(7): 8779-8802. DOI:10.3390/rs70708779

Yang, S.L., Milliman, J.D., Li, P., Xu, K., 2011. 50,000 dams later: Erosion of the Yangtze River and its delta. Global and Planetary Change, 75(1-2): 14-20. DOI:10.1016/j.gloplacha.2010.09.006

Zhang, Q., Xiao, M., Singh, V.P., Li, J., 2012. Regionalization and spatial changing properties of droughts across the Pearl River basin, China. Journal of Hydrology, 472-473: 355-366. DOI:10.1016/j.jhydrol.2012.09.054

Zhang, Q., Xu, C.Y., Chen, Y.Q.D., Jiang, J.M., 2009. Abrupt behaviors of the streamflow of the Pearl River basin and implications for hydrological alterations across the Pearl River Delta, China. Journal of Hydrology, 377(3-4): 274-283. DOI:10.1016/j.jhydrol.2009.08.026

Tables:

Table 1. Summary of Landsat data used in this study.

Study area	Period of acquisition	Number of Landsat images			Total
		Landsat 5 TM	Landsat 7 ETM+	Landsat 8 OLI	
PRD	1986-1988	109	0	0	109
	1996-1998	187	0	0	187
	2006-2008	199	202	0	401
	2016-2018	0	195	260	455
					1152
IRD	1986-1988	48	0	0	48
	1996-1998	211	0	0	211
	2006-2008	172	176	0	348
	2016-2018	0	256	292	548
					1155

Table 2. Summary of reference images from Google Earth used in this study.

Satellite	Resolution (m)	Acquisition date	Dry/wet season	Description
Pleiades-1A	0.5	2017.12.29	Dry	Overlapping spatial
WorldView-2	0.46	2017.08.20	Wet	coverage in the PRD
WorldView-2	0.46	2017.04.03	Dry	Overlapping spatial
WorldView-2	0.46	2017.08.20	Wet	coverage in the PRD
Pleiades-1A	0.5	2018.11.23	Dry	In the IRD

Figures:

Fig. 1. Location of study areas: (a) Pearl River Delta (PRD) with its eight outlets; (b) Irrawaddy River Delta (IRD) with its twelve outlets. Insets show the respective catchment areas of the two rivers.

Fig. 2. Flow chart for quantifying delta channel network changes with Landsat time-series data.

Fig. 3. Illustration of our method for mapping delta channels and calculating their widths and migrations: (a) false color composite of Landsat 8 in the IRD; (b) water occurrence frequency derived from Landsat time series from 2016-2018; (c) channel map at water occurrence threshold of 0.5; (d) channel map after removing channel bars and water bodies unconnected with channel networks, and delineation of centerlines and banklines of channel network; (e) channel width measurement at orthogonal transects; (f) Calculation of delta channel migration from centerline of 2016-2018.

Fig. 4. Channel maps derived from 1986–2018 Landsat image collection and their outlet widths during the four periods; a) the PRD; b) the IRD. The box plots show the interquartile range of channel width (box edges), the maximum and minimum channel width (whiskers), and mean channel width (shown with a dot). The Kruskal-Wallis test results are shown as *$p<0.05$; **$p<0.01$; ***$p<0.001$; ****$p<0.0001$ at the confidence level of 95%.

Fig. 5. Raw (gray) and smoothed (black) width changes over thirty-three years (1986-2018).

Fig. 6. The pattern of channel migrations in the IRD, a) regular migration; b) random migration.

Fig. 7. Position displacements between extracted and digitized river borders: (a) overestimation of water areas caused by Otsu's threshold; (b) underestimation of water areas caused by Otsu's threshold and (c) the histogram and the cumulative probability distribution of channel width errors.

Fig. 8. Comparisons of channel widths derived from digitized images from dry/wet seasons and those derived from different water occurrence. (a) Extracted banklines at different water occurrence; (b) values compared with channel widths at 0.1 water occurrence; (c) values compared with channel widths at 0.3 water occurrence; (d) values compared with channel widths at 0.5 water occurrence; (e) values compared with channel widths at 0.7 water occurrence; and (f) values compared with channel widths at 0.9 water occurrence.

Fig. 9. Annual water and sediment discharge trends in the PRD and IRD: (a) the Pearl River, calculated as the sum from the Boluo, Shijiao, and Gaoyao stations; (b) the Irrawaddy River at Pyay station (1966–1996) and Magway station (1990–2010).

Fig. 10. Riparian tideland reclamation and water level rise from 1986 to 2018 in four Pearl River estuaries: (a) Hengmen; (b) Modaomen; (c) Jitimen; and (d) Hutiaomen.

Fig. 11. Narrow channel extraction from (a) single image using Otsu's thresholding method; (b) water occurrence composite image; (c) 0.5 water occurrence frequency derived from Landsat time-series image and (d) 0.5 water occurrence frequency derived from Sentinel-2 time-series images.

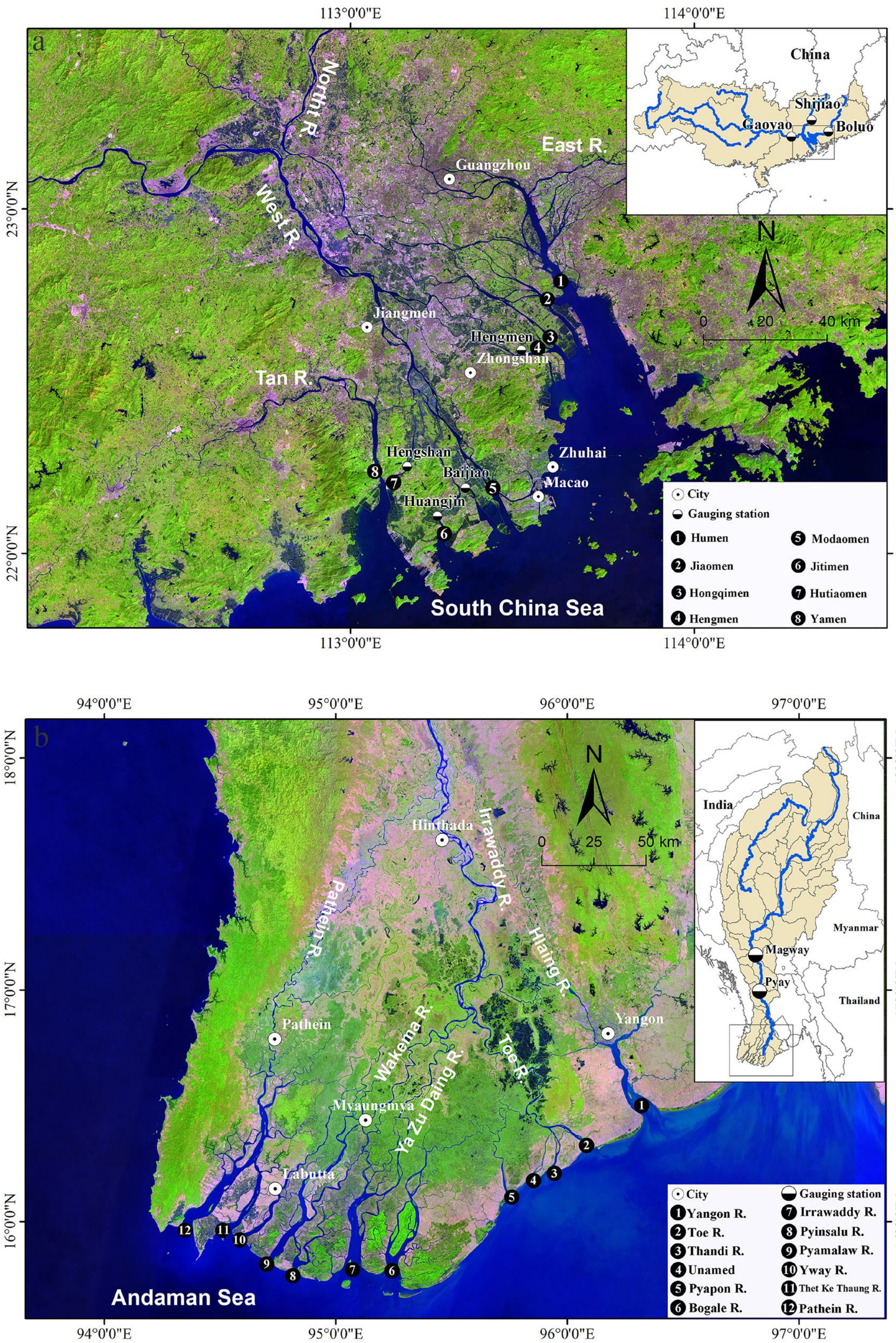
a
113°0'0"E
114°0'0"E
23°0'0"N
22°0'0"N
North R.
West R.
East R.
Tan R.
Guangzhou
Jiangmen
Hengmen
Zhongshan
Hengshan
Baijiao
Huangjin
Zhuhai
Macao
South China Sea
China
Shijiao
Gaoyao
Boluo
N
0 20 40 km
City
Gauging station
1 Humen
2 Jiaomen
3 Hongqimen
4 Hengmen
5 Modaomen
6 Jitimen
7 Hutiaomen
8 Yamen
b
94°0'0"E
95°0'0"E
96°0'0"E
97°0'0"E
18°0'0"N
17°0'0"N
16°0'0"N
Hinthada
Irrawaddy R.
Pathein R.
Hlaing R.
Yangon
Pathein
Wakema R.
Toe R.
Ya Zu Daing R.
Myaungmya
Labutta
Andaman Sea
N
0 25 50 km
India
China
Myanmar
Thailand
Magway
Pyay
City
Gauging station
1 Yangon R.
2 Toe R.
3 Thandi R.
4 Unamed
5 Pyapon R.
6 Bogale R.
7 Irrawaddy R.
8 Pyinsalu R.
9 Pyamalaw R.
10 Yway R.
11 Thet Ke Thaung R.
12 Pathein R.

Figure 1

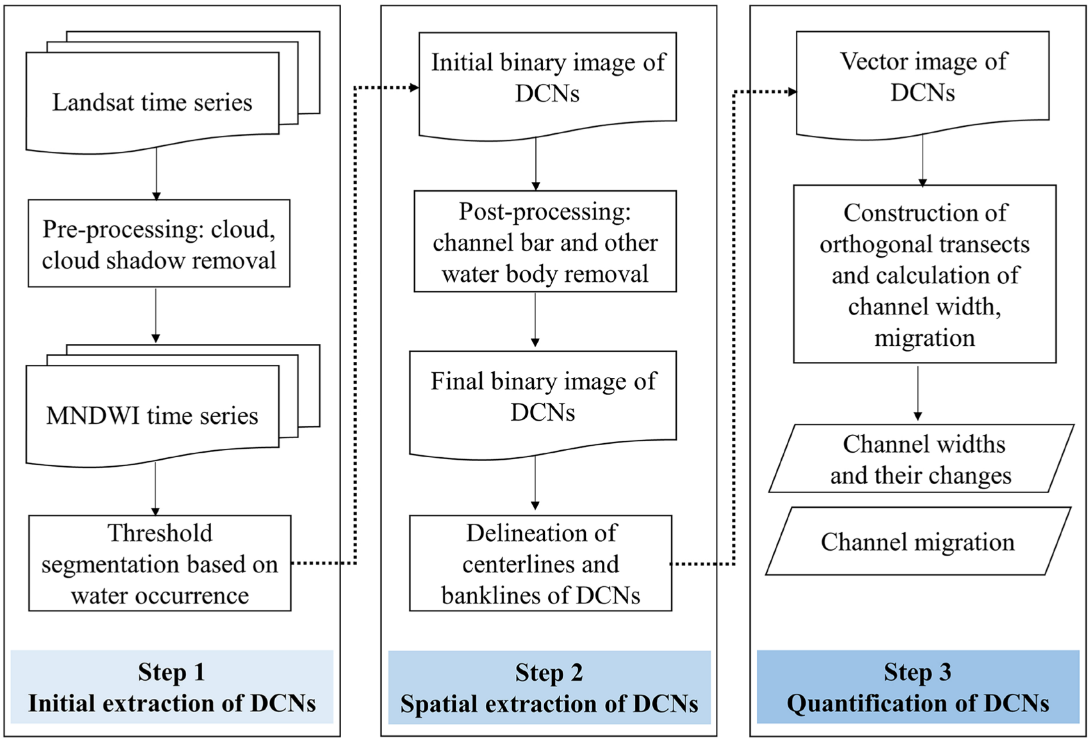

Figure 2

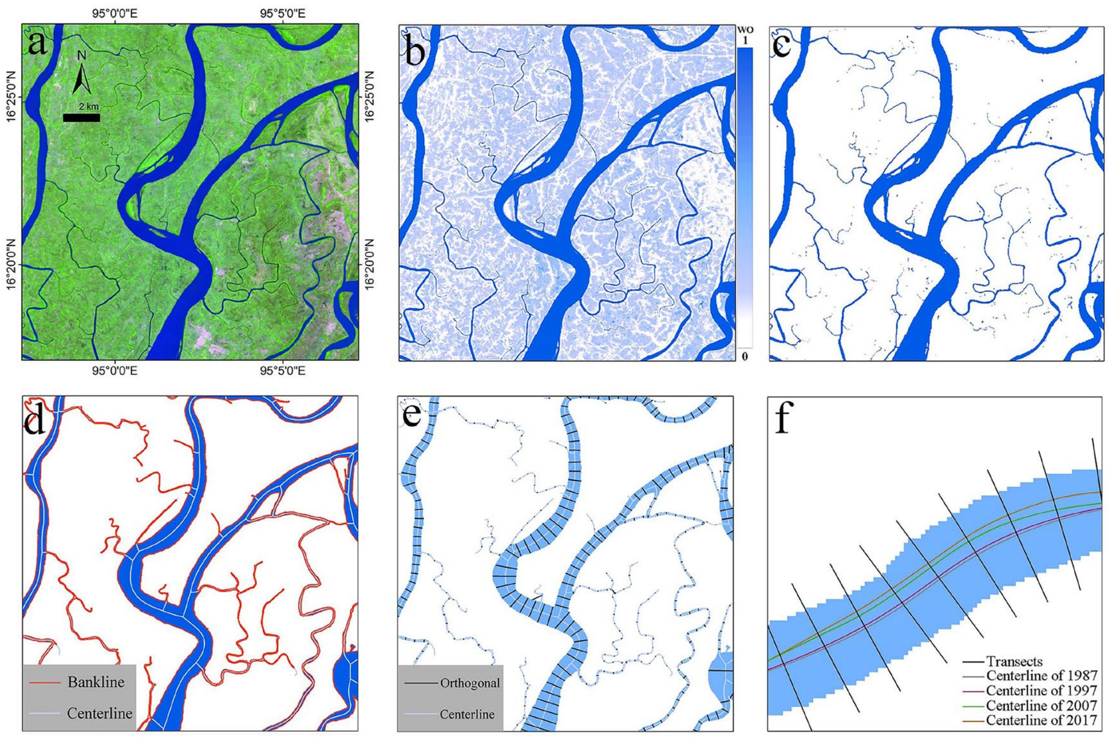

Figure 3

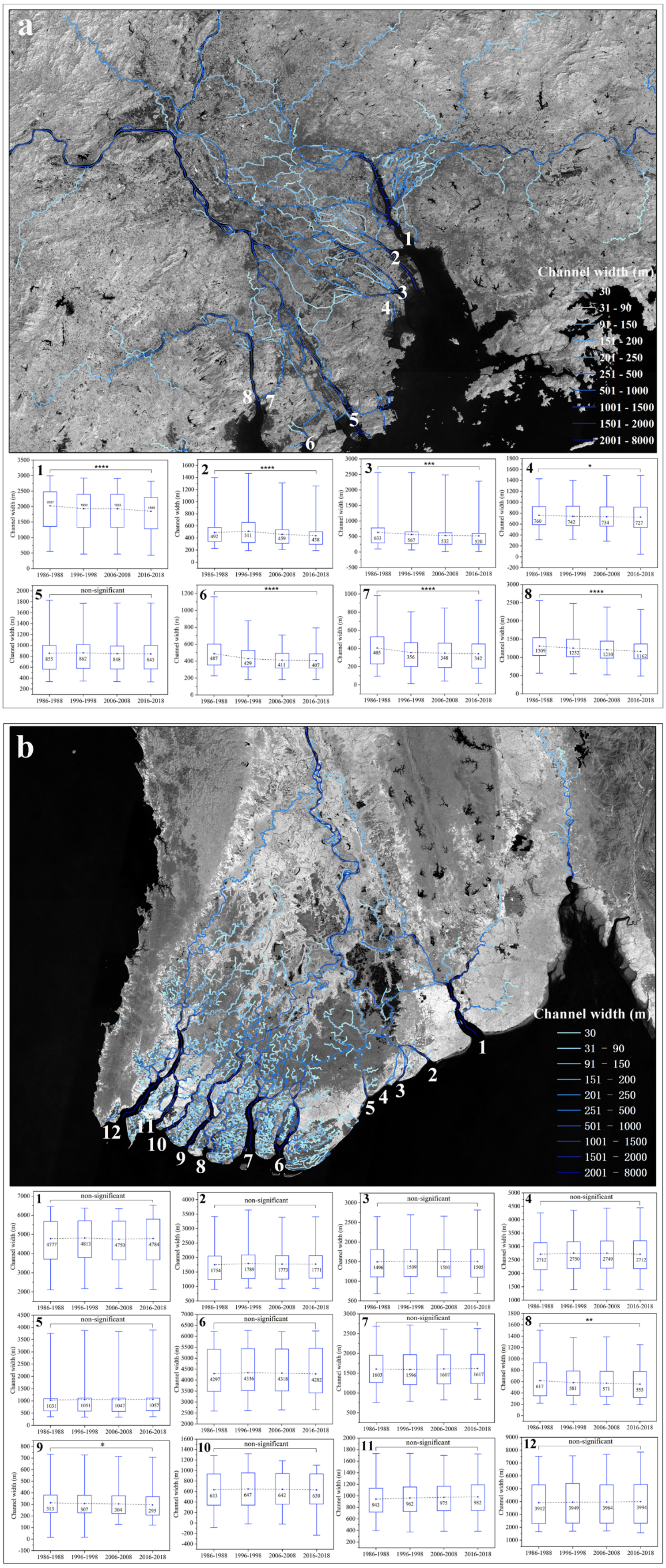
a
Channel width (m)
30
31 - 90
91 - 150
151 - 200
201 - 250
251 - 500
501 - 1000
1001 - 1500
1501 - 2000
2001 - 8000
1 2 3 4 5 6 7 8
Channel width (m)
1986-1988 1996-1998 2006-2008 2016-2018
non-significant
b
Channel width (m)
30
31 - 90
91 - 150
151 - 200
201 - 250
251 - 500
501 - 1000
1001 - 1500
1501 - 2000
2001 - 8000
1 2 3 4 5 6 7 8 9 10 11 12
non-significant

Figure 4

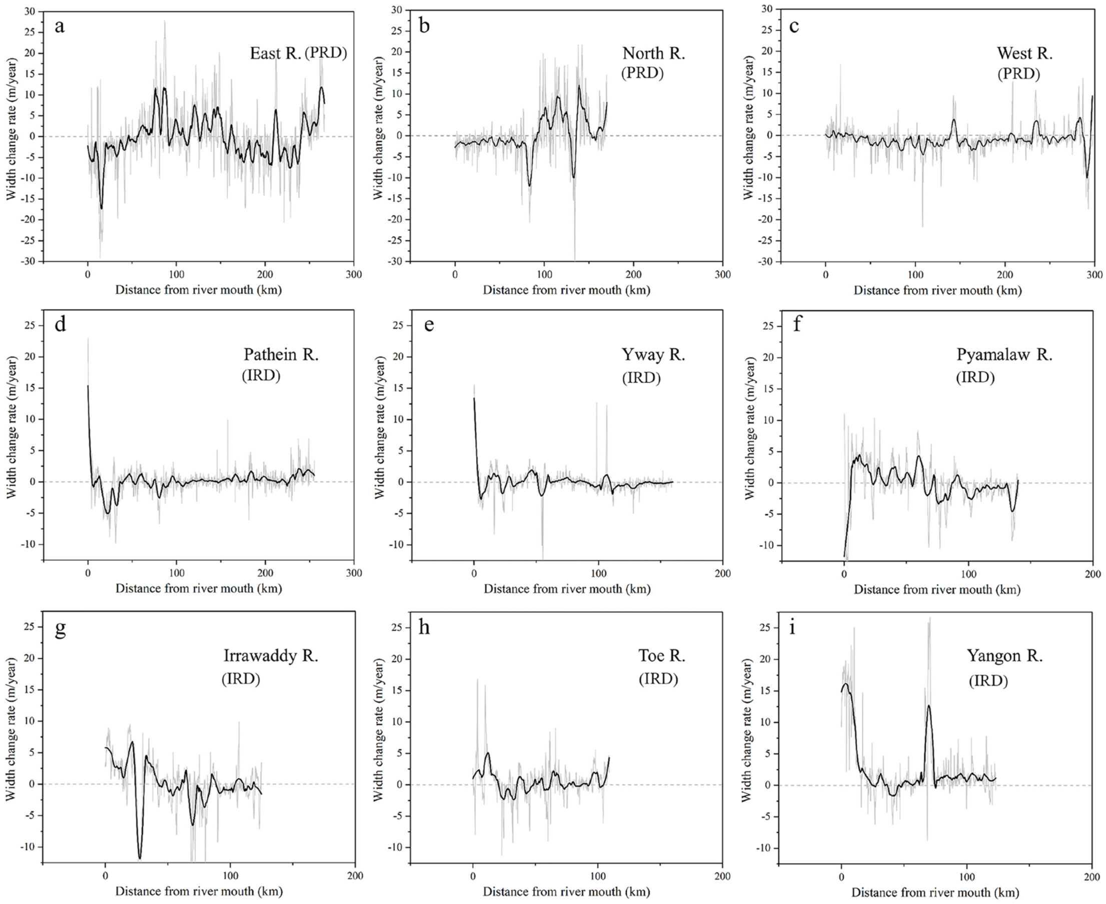

Figure 5

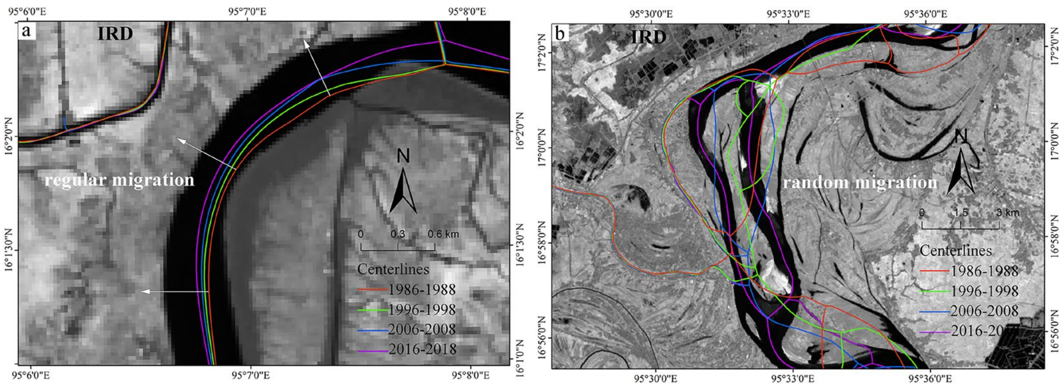

Figure 6

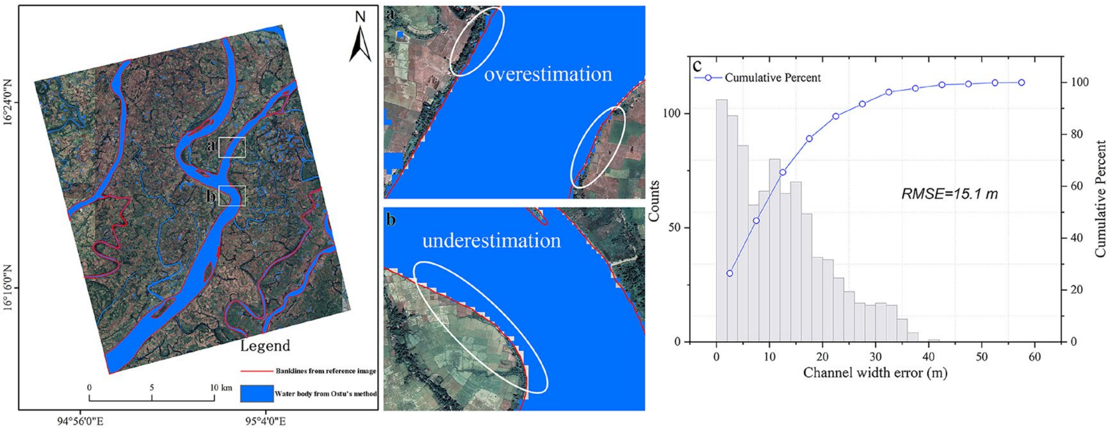

Figure 7

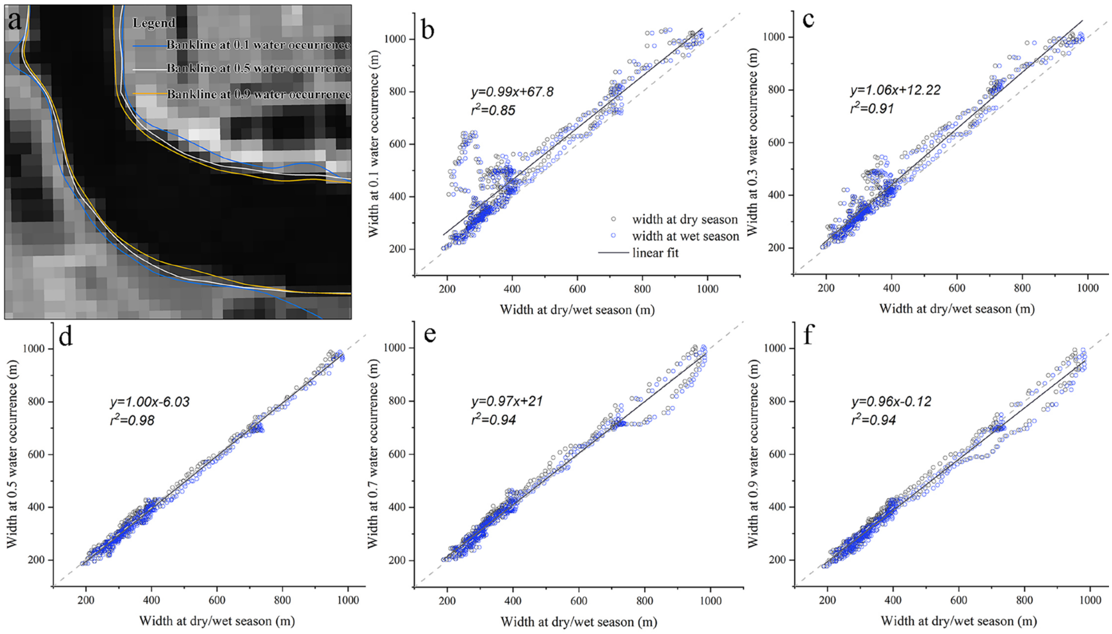

Figure 8

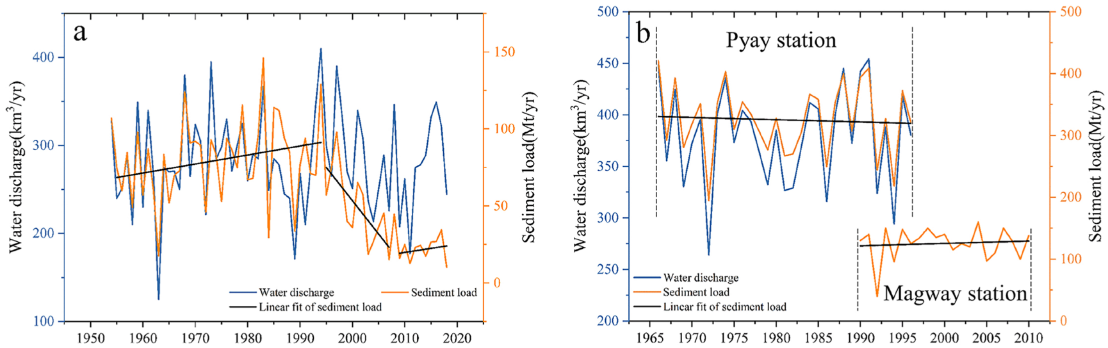

Figure 9

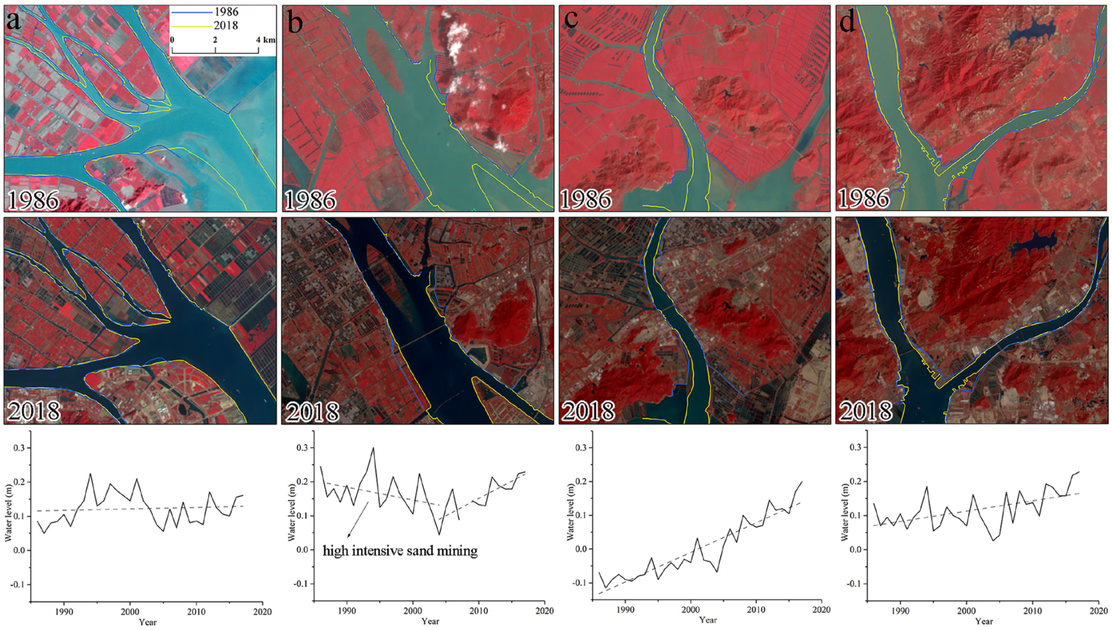

Figure 10

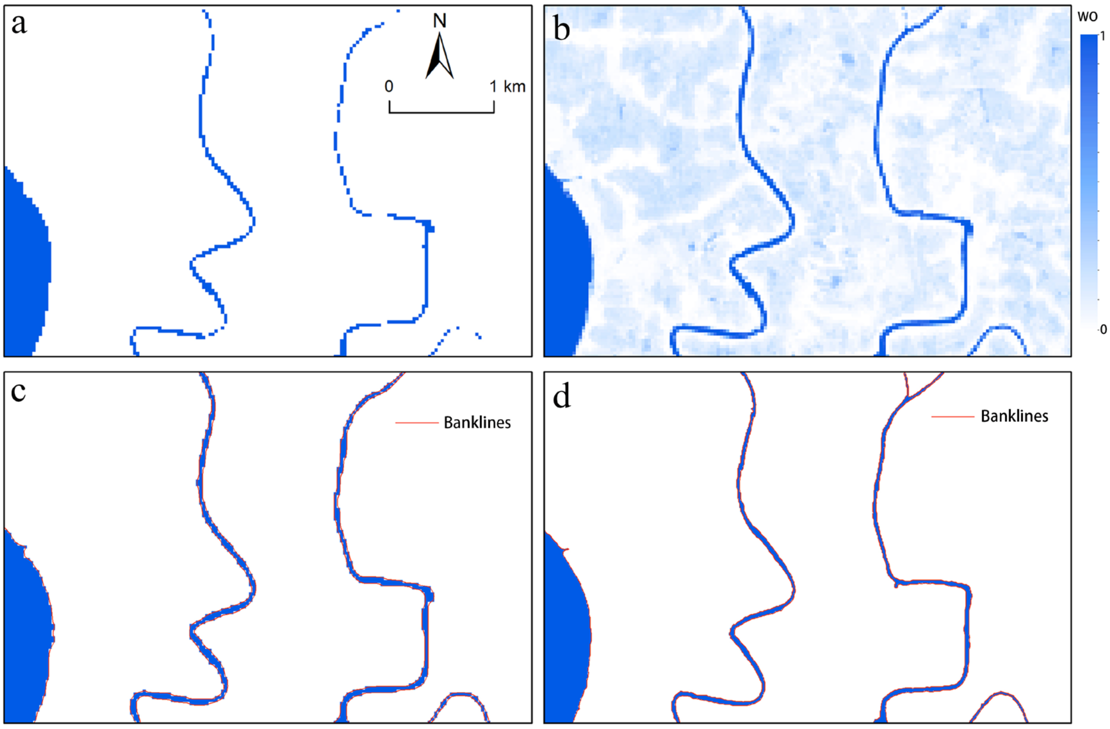

Figure 11